



Wetting and other physical characteristics of polycarbonate surface textured using laser ablation

B.S. Yilbas^{a,*}, M. Khaled^b, N. Abu-Dheir^a, N. Al-Aqeeli^a, S.A.M. Said^a, A.O.M. Ahmed^b, K.K. Varanasi^c, Y.K. Toumi^c

^a ME Department, King Fahd University of Petroleum & Minerals, Dhahran, Saudi Arabia

^b CHEM Department, King Fahd University of Petroleum & Minerals, Dhahran, Saudi Arabia

^c Mechanical Engineering, Massachusetts Institute of Technology, Boston, USA

ARTICLE INFO

Article history:

Received 29 April 2014

Received in revised form 12 July 2014

Accepted 9 September 2014

Available online 21 September 2014

Keywords:

Polycarbonate glass

Laser ablation

Hydrophobicity

Residual stress

ABSTRACT

Surface texturing of polycarbonate glass is carried out for improved hydrophobicity via controlled laser ablation at the surface. Optical and physical characteristics of the laser treated layer are examined using analytical tools including optical, atomic force, and scanning electron microscopes, Fourier transform infrared spectroscopy, and X-ray diffraction. Contact angle measurements are carried out to assess the hydrophobicity of the laser treated surface. Residual stress in the laser ablated layer is determined using the curvature method, and microhardness and scratch resistance are analyzed using a micro-tribometer. Findings reveal that textured surfaces compose of micro/nano pores with fine cavities and increase the contact angle to hydrophobicity such a way that contact angles in the range of 120° are resulted. Crystallization of the laser treated surface reduces the optical transmittance by 15%, contributes to residual stress formation, and enhances the microhardness by twice the value of untreated polycarbonate surface. In addition, laser treatment improves surface scratch resistance by 40%.

© 2014 Elsevier B.V. All rights reserved.

1. Introduction

Adhesion of dust onto surfaces results in a loss of optical transmittance from transparent/semi-transparent surfaces and remains a challenging problem for solar applications. In photovoltaic applications, optical transmittance of the protecting glass becomes critical issue to sustain efficiency and output power of the photovoltaic cells over long periods. Although a glass layer protects the photoactive area from environmental hazardous, dust accumulation at the glass surface lowers device efficiency and the output power in the long term because of the reduced optical transmittance. Similarly, in solar thermal applications dust accumulation on mirrors has significant negative impact on performance. This situation becomes significantly important in the areas where dust accumulation is unavoidable such as dry and desert environments. One of the solutions to prevent or minimizing the dust accumulations at the protective glass surfaces is to texture the surface for enhancing hydrophobic while creating a self-cleaning effect at the surface. Superhydrophobic surfaces have been shown to have remarkable water-repelling and self-cleaning properties [1–6]. To

improve hydrophobic characteristics, nano/micro texturing of the surface becomes necessary, similar to the surfaces that are widely observed in nature, such as lotus leaves, rice leaves, red rose petals, fish scales, etc. [7–12]. Many techniques and processes have been developed to enhance the hydrophobicity of surfaces [13–21]; however, some of these techniques involve multi-step procedures and harsh conditions or required specialized reagents and equipment. Some of these techniques include phase separation [13], electrochemical deposition [14], plasma treatment [18], sol-gel processing [19], electrospinning [20], and solution immersion [21]. In addition, surface free energy of substrate materials can be modified through altering chemical composition at the surface via chemical and physical reactions, and introducing coating or alloying elements. Micro/nano texturing of surfaces have many challenges in terms of cost, processing time, equipment, and skilled man power requirements; however, it was demonstrated that laser controlled ablation can be used effectively to texture surfaces at micro/nano levels [22]. Since laser surface processing involves precision operation and non-mechanical contact, mechanical and chemical defects can be minimized at the surface with considerably high processing speed. Although laser controlled ablation has several advantages over the conventional surface texturing processes, thermal effects on textured surfaces, and optical and mechanical characteristics need to be examined in detail,

* Corresponding author. Tel.: +966 38604481; fax: +966 38602949.
E-mail address: bsyilbas@kfupm.edu.sa (B.S. Yilbas).

particularly, to achieve desired surface textures pertinent to improve hydrophobicity for photovoltaic applications.

Polycarbonate glass is one of the candidates to replace silicon base protective glasses for photovoltaic applications. This is because of its high transmission of solar radiation, low density, high fracture toughness, and mechanical flexibility. However, polycarbonate glass surface is hydrophilic and it is hard to repel accumulated dust particles from the surface [23]. Since dust accumulation at the protective glass surface reduces the solar radiation energy reaching the photovoltaic surface, preventing dust accumulation at the protective glass surface becomes necessary to improve solar transmission. This can be achieved via texturing a polycarbonate glass surface while creating a hydrophobic affect. It should be noted that reduced transmission efficiency (as defined through the solar energy reaching at the photovoltaic active surface area over the solar energy reaching at the protective glass surface) lowers photovoltaic device output power. Utilizing chemical or thermal processes to texture polycarbonate glass via crystallization reactions have advantages over other texturing methods such as mechanical texturing. This is because of chain flexibility of polycarbonate molecules in the glass structure, which presents high crystallization ability when subjected to solvents such as acetone [23]. Considerable research studies were carried out to examine hydrophobicity improvement for polycarbonate surfaces [24–31]. The effects of crystallization on hydrolytic stability of polycarbonate were studied by Zhou et al. [24]. They demonstrated that the surface-crystallized polycarbonate glass had better hydrolytic stability than amorphous polycarbonate glass because of: (i) the reduced rate of the elongation at break of surface-crystallized polycarbonate glass, which was much smaller than that of amorphous polycarbonate glass during hydrolysis, (ii) the impact strength of amorphous polycarbonate glass reduced rapidly in the early stage of hydrolysis, (iii) the stability of the chemical structures of surface-crystallized polycarbonate glass, which was higher than that of amorphous polycarbonate glass during hydrolysis, resulting in fewer changes in the glass transition temperature. A new chemical technique for preparation of superhydrophobic polymer surfaces was introduced by Yilgor et al. [25]. They indicated that a spin-coated parent polymer by a dilute solution containing hydrophobic silica and polymer forming tetrahydrofuran thin film resulted in rough surfaces with homogeneously distributed silica particles in 1–10 μm range and the coated surfaces displayed superhydrophobic characteristics with large contact angles and low hysteresis. Superhydrophobic and superhydrophilic polycarbonate glasses by tailoring chemistry and nano-texturing due to plasma processing were studied by Palumbo et al. [26]. They showed that etching process allowed for formation of nanopillars tens of nanometers wide and up to a micrometer high, which were responsible for a unique behavior of the surface. Hierarchical polymeric textures through solvent-induced phase transformation were examined by Cui et al. [27]. The findings revealed that crystallization of the polymer led to the formation of a hierarchical structure composed of microporous spherulites covered with nano-fibrils, which in turn resulted in superhydrophobic wetting behavior. Forming a superhydrophobic polycarbonate fiber network from hydrophilic polycarbonate through electrospinning was studied by Li and Barber [28]. They indicated that complex surface geometries were obtained after the process, which in turn improved the wetting behavior of polycarbonate fiber network. A method for creating superhydrophobic polymer surfaces was introduced by Hurst et al. [29]. The method combined sanding and reactive ion etching treatment of the polymer surface generating micro and nanoscale surface roughness, which was followed by subsequent coating of a fluorinated silane molecule modifying the surface chemistry. They indicated that the resulting polymer surfaces retained their superhydrophobicity over long periods while

demonstrating the stability of the micro and nanoscale surface roughness and the hydrophobic surface coating. Superhydrophobic surfaces, from hydrophobic or hydrophilic polymers via nanophase separation or electrospinning/electrospraying, were investigated by Papadopoulou et al. [30]. They demonstrated that the films, produced by hydrophilic polymers via electrospinning/electrospraying method, were hydrophobic and a narrow contact angle range was observed. However, films produced by the same polymers and their blends via phase separation presented a wide range of contact angles in contrast to the case of hydrophobic polymers. The findings, therefore, revealed that the detrimental role of random surface morphology on contact angle values could be counterbalanced by the inherent hydrophobicity of the polymer. Nanocarbon-induced rapid transformation of polymer surfaces into superhydrophobic surfaces was studied by Han et al. [31]. The method consisted of dipping polymer sheets in a solvent in which the polymer was partially soluble and then inducing solution crystallization by dipping the sheet in a poor solvent for several seconds. They demonstrated that the resulting surfaces had superhydrophobic features.

Although crystallization of polycarbonate glass provides micro/nanosize textures at the surface, once the crystallization is completed surface morphology and attenuation characteristics of the crystallized surface change because of the rigidity of molecular chains in the crystalline structure [23]. Consequently, optical transmittance reduces considerably for the crystallized surface despite the hydrophobicity of the surface increases significantly. Although laser ablation of polycarbonate surface triggers crystallization process because of the thermal effects, this undesirable effect may be minimized under the high speed and controlled ablation process. In addition, laser treatment alters the mechanical properties of the treated section; such as microhardness enhancement at the surface and residual stress formation in the treated layer. Nevertheless, laser control ablation can minimize the changes in the mechanical properties and, at the same time, it can form a surface texture improving the hydrophobicity. In the present study, laser texturing of polycarbonate glass via laser controlled ablation is presented. Topology, hydrophobicity and mechanical characteristics of the ablated surfaces are examined using the analytical tools. Mechanical characteristics include microhardness, scratch resistance, and micro-stresses are presented. The analytical tools used include optical, scanning electron, and atomic force microscopes, X-ray diffraction, Fourier transform spectroscopy, micro-tribometer, and goniometer.

2. Experimental

Polycarbonate glass of 3 mm thickness was used as workpieces. Polycarbonate glass was derived from A PBA (p-hydroxyphenyl) and it had excellent optical clarity with high toughness. The CO_2 laser (LC-ALPHAIII) delivering nominal output power of 2 kW was used to irradiate the workpiece surface. The nominal focal length of the focusing lens was 127 mm. The laser beam diameter focused at the workpiece surface was ~ 0.25 mm. Argon assisting gas emerging from the conical nozzle and co-axially with the laser beam was used. Laser treatment tests were repeated several times by incorporating different laser parameters and laser treatment parameters led to the desired surface quality in the sense of wetting were selected. The details of laser treatment process are given in [22]. Laser treatment conditions are given in Table 1.

Material characterization of the laser treated surfaces was carried out using optical microscope, SEM, AFM, and XRD. Jeol 6460 electron microscopy is used for SEM examinations and Bruker D8 Advanced having $\text{CuK}\alpha$ radiation is used for XRD analysis ($\lambda = 1.54180 \times 10^{-10}$ m). A typical setting of XRD was 40 kV and 30 mA and scanning angle (2θ) was ranged 10° – 60° . Surface

Table 1
Laser treatment conditions used in the experiment.

Scanning speed (mm/min)	Peak power (W)	Frequency (Hz)	Nozzle gap (mm)	Nozzle diameter (mm)	Focus setting (mm)	Argon pressure (kPa)
600	2000	1500	1.5	1.5	127	600

roughness measurement of the laser-melted surfaces was performed using a 5100 AFM/SPM Microscope by Agilent in contact mode. The tip was made of silicon nitride probes ($r=20\text{--}60\text{ nm}$) with a manufacturer specified force constant, k , of 0.12 N/m .

Microphotonic digital microhardness tester (MP-100TC) was used to obtain microhardness at the surface of the nitride layer. The standard test method for Vickers indentation hardness was adopted (ASTM C1327-99). Microhardness was measured at the workpiece surface prior and after the laser treatment process. The measurements were repeated five times at each location for the consistency of the results.

A linear micro-scratch tester (MCTX-S/N: 01-04300) was used to determine the friction coefficient and scratch resistance of the laser treated and untreated surfaces. The equipment was set at the contact load of 0.03 N and end load of 5 N . The scanning speed was 5 mm/min and loading rate was 5 N/s . The total length for the scratch tests was 5 mm .

Nicolet Nexus 670 FT-IR Spectrometer from Thermo Electron Corporation was used for FTIR responses of the surface. The equipment was built on a common optical and electronics platform which made it easy to use. The wetting experiment was performed using Kyowa (model – DM 501) contact angle goniometer. A static sessile drop method was considered for the contact angle measurement. The water contact angle between the water droplet and the heat treated surface was measured with the fluid medium as de-ionized water. Droplet volume was controlled with an automatic dispensing system having a volume step resolution of $0.1\text{ }\mu\text{l}$. Still images were captured, and contact angle measurements were performed after one second of deposition of water droplet on the surface.

Residual stress measurement was carried out using the curvature method. The deflection of the workpiece during laser scanning was recorded and the final deflection was measured using the optical imaging technique. The equation relating deflection Δx to curvature κ is obtained from the geometric relation, which yields [32]:

$$\kappa = \frac{1}{R} = \frac{L_{\text{arc}}}{\cos^{-1}(1 - (\Delta x/R))} \quad (1)$$

where L_{arc} is the arc length of the specimen, R is the curvature radius and Δx is the final deflection due to curvature. The Stony equation [32] is used to obtain the relationship between the residual stress (σ) and the curvature [32]:

$$\sigma = \frac{\kappa E_s t_s^2}{6(1 - \nu_s) t_c} \quad (2)$$

where E_s is the elastic modulus, t_s is workpiece thickness, ν_s is the Poisson's ratio of the polycarbonate glass, and t_c is the laser treated layer thickness, which is measured from SEM images.

Scratch resistance of the laser treated and untreated surface was determined from the standard test method in line with the ASTM D7027-05 standard. The linear micro-scratch tester (MCTX-S/N: 01-04300 [9]) and scratch hardness measurement data were incorporated in the calculations. According to ASTM D7027-05 standard, scratch hardness (H_s) can be defined as:

$$H_s = \frac{4qP}{\pi w^2} \quad (3)$$

where P is the normal load used in the scratch tests in Newton, w is the scratch width in millimeters, q is the dimensionless parameter, which depends on the extend of elastic recovery of the polymer during scratching. In this case, full elastic recovery implies $q=1$ while no recovery implies $q=2$.

3. Results and discussion

Surface texturing of polycarbonate glass via controlled laser ablation is carried out for improved surface hydrophobicity. Thermal, optical, and mechanical characteristics of the textured surfaces are examined incorporating the analytical tools.

3.1. Thermal effects and crystallinity

Fig. 1 shows optical and SEM micrographs of the laser treated surface. Laser treated surface is free from large scale asperities such as large size cracks and voids. Although surface treatment takes place at a constant laser scanning speed, no regular textured patterns are observed at the surface unlike laser ablation of ceramic surfaces [22]. This is associated with the shallow cavity formation under the controlled ablation at the surface. It should be noted that repetitive pulses with 1500 Hz pulsing frequency are incorporated during the laser ablation process. In this case, overlapping of the irradiated spots due to laser repetitive pulses, results in formation of continuous laser scanning tracks, which consist of fine cavities and re-solidified sections at the surface. Since laser beam intensity is Gaussian at the workpiece surface, peak intensity occurs at the irradiated spot center. The cavity is formed at the central region of the irradiated spot and melting takes place in the cavity vicinity due to the low laser intensity in this region. However, repetitive laser pulses modify this structure at the surface because of the molten flow from the recently formed cavity neighborhood to the previously formed cavity. Therefore, surface texture is modified and micro/nano pores are formed at the surface. It is evident from optical image (Fig. 1a) that crystal growth extends radially from the potential nucleation site; however, widespread branching is not visible in the frame of the radial growth. In addition, in some regions (Fig. 1a), intermittent branching takes place, which can be considered as a hallmark of growth to form large spherules. The fine size cavity formation is also observed in Fig. 1b. Since high pressure argon is used as assisting gas, no sideways burning through oxidation reactions are observed at the ablated surface. Surface texture composed of micro/nano features is evident from the high magnification SEM micrograph (Fig. 1a). Partially formed spherules with varying diameters are also observed from optical and SEM micrographs (Fig. 1b); however, they do not form hierarchical structure at the surface (Fig. 1c and d). This is associated with the varying nucleation density due to non-uniform cooling rates at the surface. Although crystal size varies at the surface, large size crystals do not form due to the high cooling rates unlike those reported for other crystallization processes [23,33]. Fig. 2 shows SEM micrographs of the cross-section of the laser textured layer. Laser treated layer consists of fine structures emanating from the surface (Fig. 2a). The laser treated layer extends almost uniformly along the workpiece surface with the thickness of about $1.8\text{ }\mu\text{m}$ (Fig. 2b) and crystal structures formed in the surface region during the solidification process (Fig. 2c). The fine cavities formed at the surface results

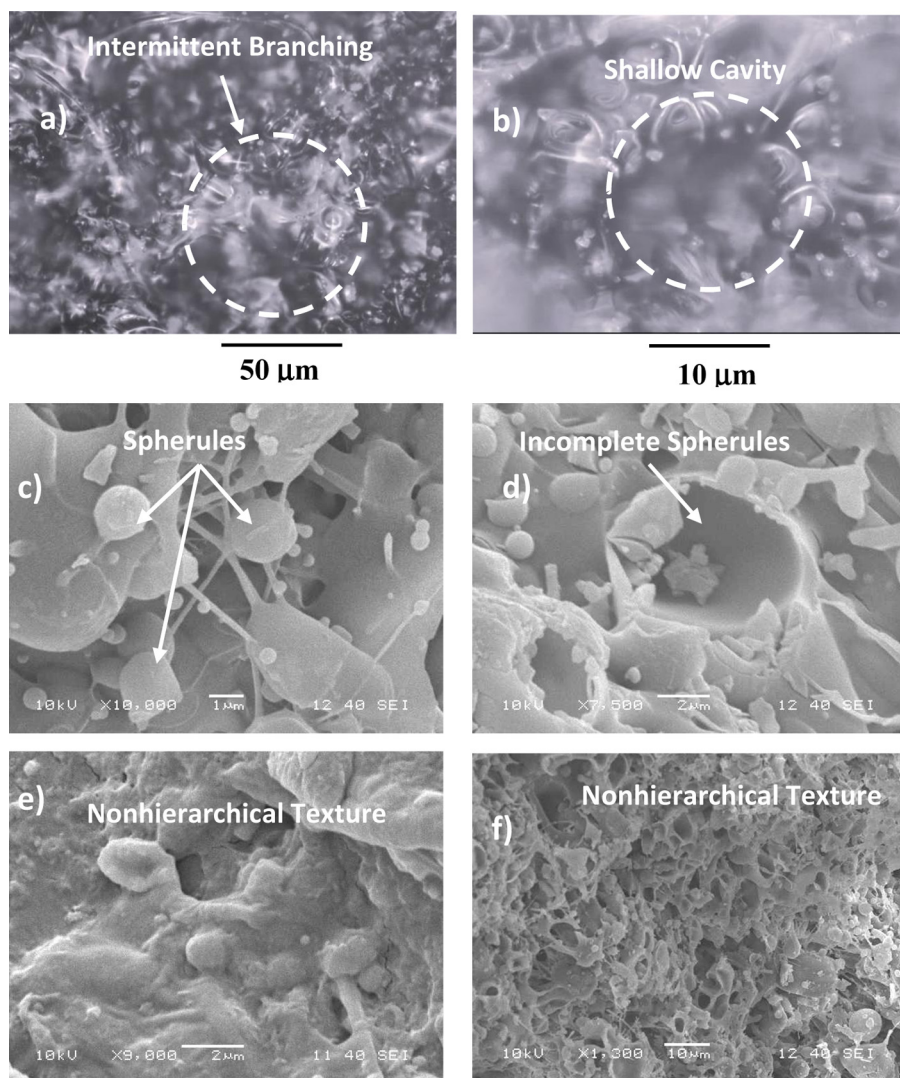


Fig. 1. Optical images and SEM micrographs of laser treated surface: (a) optical image demonstrating the crystals formed at the surface and radial growth of crystals and intermittent branching, (b) laser produced fine size shallow cavity and spherules, (c) spherules formed at the surface, (d) incomplete spherules, and (e and f) nonhierarchical texture.

in micro/nano level waviness contributing to the overall surface texture of the laser treated layer (Fig. 2d).

Laser surface ablation accompanied with rapid evaporation at the surface during the repetitive pulse heating process. Although the heating duration is short, thermal effects are introduced into the irradiated region. This, in turn, results in thermally-induced stresses and crystallization of the irradiated surface. In general, crystallization takes place in three stages including initiation of crystallization, primary crystallization, and secondary crystallization [34]. During crystallization, a nucleus emerges when the polymer chains align in a parallel way and as the process progresses gradually, the chains are added to the nucleus. Once the nucleus reaches to the critical size growth becomes spontaneous [34]. The nucleation leads the formation of bundle-like or lamellar crystals; however, the difference between the types of crystallization is length of primary nucleus and free energy of the surface normal to the chain direction per unit area [35]. Since laser surface ablation results in fine melt layer formed at the ablated surface during the process, crystallization mainly starts from the molten state. In this case, the mixture of bundle-like and lamellar nucleus can be formed due to the series of additions of the repeating units during the solidification. The free energy per unit volume $\Delta\mu$, ($\Delta\mu = \Delta h_f \Delta T / T_m$ where ΔT is the temperature difference,

$\Delta T = T_m - T$, T_m is the melting temperature and T is the temperature of the molten polycarbonate glass, and Δh_f is the heat of fusion per unit volume of the crystal) becomes important for the crystal size [36]. Since the length of a crystal (l) is associated with the free energy per unit volume ($\Delta\mu$) and the free energy of the surface normal to the chain direction per unit area (σ_e) [37], the crystal size can be approximately expressed as $l = 2\sigma_e / \Delta H_0 (1 - (T_m / T_m^0))$ [38]. Introducing the heat of fusion per unit volume of totally crystalline ΔH_0 is $0.11 \times 10^9 \text{ J/m}^3$, the surface energy (σ_e) is 0.094 J/m^2 , the melting temperature of 155°C , and the equilibrium melting temperature (T_m^0) 318°C [38], the lamellar thicknesses can be estimated as 87 \AA . The lamellar thickness estimated differs slightly from the previous finding, which is 73 \AA [38]. The difference is associated with the high cooling rates and possible non-equilibrium processes takes place during the crystallization due to laser pulsation at the surface, which is in the order of seconds, during the ablation process. However, solidification process related to the post laser ablation involves non-uniform cooling at the surface, which in turn affects the crystal growth and crystal size in the re-solidified region. Moreover, a polymer crystal is heated toward its melting temperature and undergoes significant lattice expansion, the average inter-chain distances increase, facilitating motion of conformation defects within the crystal lattice. Two supporting factors

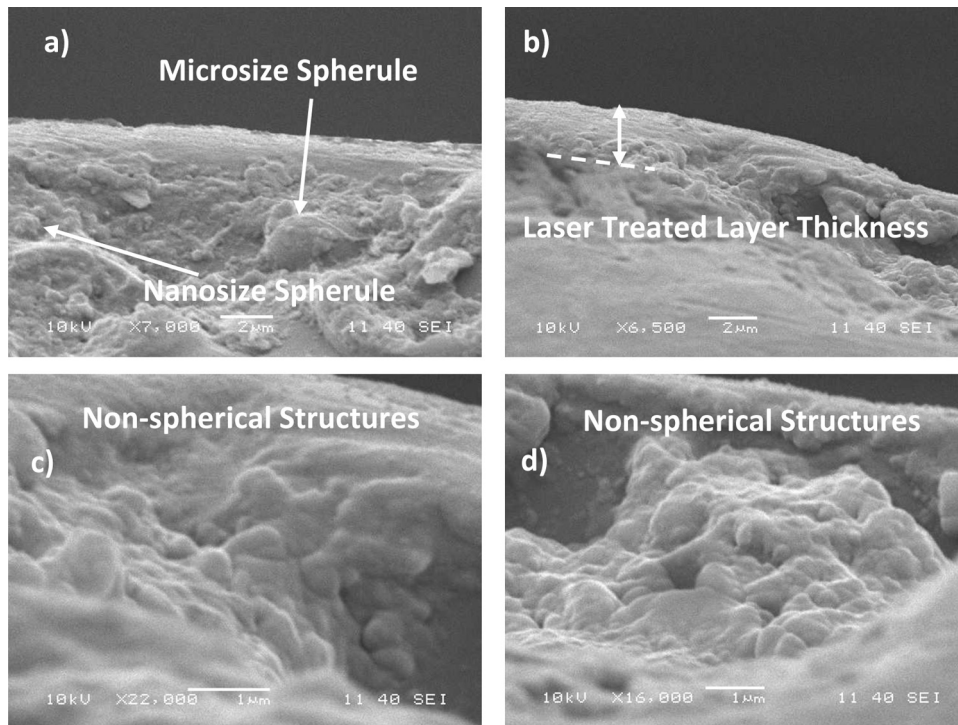


Fig. 2. SEM micrographs of cross-section of the laser treated layer: (a) spherules at different sizes, (b) laser treated layer thickness ($\sim 1.8 \mu\text{m}$), (c) non-spherical structures initiating the formation of spherules, and (d) non-spherical dense structure.

have been given to justify the possibility of lamellar thickening during crystallization at high temperatures [39]. The first is that polymer crystals are less dense at higher temperatures and polymer chains in the crystalline phase have increased mobility so local changes in segmental conformation can take place. This can give rise to an increase lamellar thickness, hence, a decrease in crystal free energy. Secondly, as the annealing temperature increases, the critical primary nucleus size and the lamellar thickness of minimum stability increase. However, when annealing temperatures are higher than the crossover temperature, the thickness of amorphous layer between lamellae may not be large enough to allow for the formation of new crystals or the sequence of polymer segments available for crystallization in the inter-lamellar amorphous fraction may be too short to form a stable crystal between the primary lamellae [40]. The secondary crystallization process have shown that, despite all expectations, the isothermal lamellar thickening process is possible [41]; however, at high temperatures, secondary crystals do not form by the chain folding mechanism, but rather by a local bundling of chain sequences into ordered structures of reduced lateral dimensions. Crystallization at the surface is also evident from X-ray diffraction pattern, which is shown in Fig. 3. X-ray diffraction pattern is also given for the untreated surface for the comparison reasons. The X-ray diffractogram demonstrates that the untreated substrate is totally amorphous; in which case, there is no clearly identifiable peak occurs in the diffractogram. The position of the diffraction peaks in the diffractogram for the laser treated surface reveals that mainly three peaks are visible, which correspond to the diffraction angle 17.1° (020) phase, 21.5° (213) phase, and 25.7° (222) phase. However, peak heights and full width at half maximum (FWHM) of the peak differ for each in the diffractogram. The crystallinity of the laser treated surface can be determined from the ratio of the sum of integrated intensities of the reflections from the crystalline phases (peaks) to the total scattered intensity after background subtraction [38]. This arrangement results in the crystallinity (f_c) values in the order of 18%, which is significantly higher than that reported for other crystallization methods. Consequently,

melting and solidification result in large crystallinity at the surface during the ablation process.

Fig. 4 shows FTIR data obtained for the laser treated and untreated samples. Untreated sample shows absorption spectrum of a typical polycarbonate glass [42]. The absorption bands are related to C–H bond stretching vibration taking place on $2874\text{--}2969 \text{ cm}^{-1}$ and $860\text{--}680 \text{ cm}^{-1}$ band corresponds to bending vibration of C–H bond. The band observed on 1496 cm^{-1} is related to C–H bending vibrations of methylene groups. In addition, aromatic C–H bending vibration takes place on $860\text{--}680$ and aromatic C=C bending vibration occurs on $1700\text{--}1500 \text{ cm}^{-1}$. In addition, 1770 cm^{-1} corresponding to C=O stretching vibrations band of ethers. The absorption characteristics of the laser treated surface indicate that absorption increases at certain wavelengths. This can be explained in terms of crystallinity induction polymer chains, which are more closely packed and can cause restriction group vibration while causing band intensity increase in the absorption spectrum. Consequently, closely packed polymer chains contribute

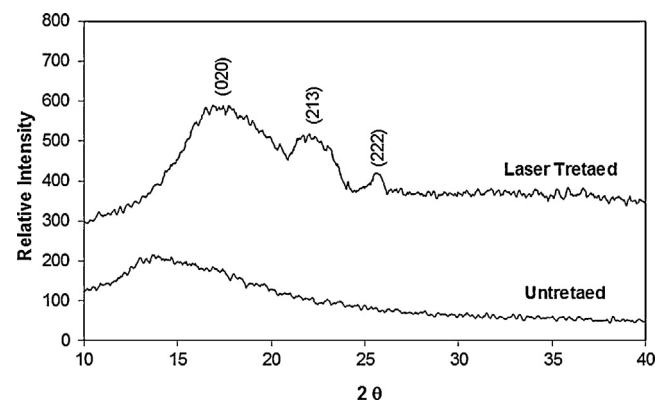


Fig. 3. X-ray diffractograms of laser treated and untreated workpieces.

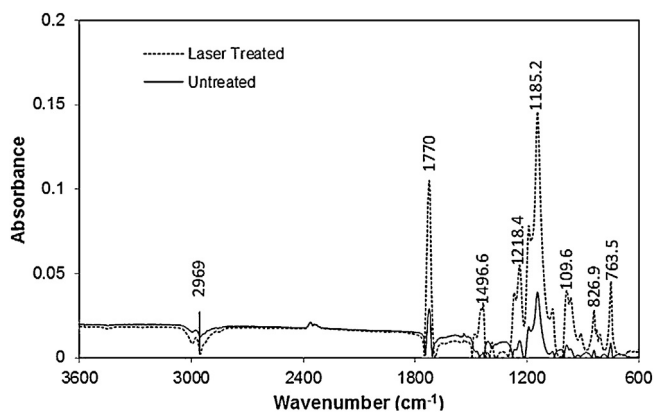


Fig. 4. FTIR spectra of laser treated and untreated workpieces.

to the residual stress increase and the micro-hardness enhancement in the laser treated layer.

3.2. Mechanical characteristics

Mechanical characteristics of the textured surfaces include microhardness, scratch resistance, and residual stress formation because of thermally induced micro-stresses and crystallization at the surface.

Residual stress formed in the treated layer is determined from the curvature technique. Residual stress obtained from the curvature method is in the order of -26 MPa and the findings reveal that residual stress is compressive. The formation of residual stress is associated with the thermal effect due to high cooling rates and crystallization of the laser treated surface; in which case, molecular structures are modified in the crystal structure while causing the stresses formation after completion of the crystallization process [43]. It should be noted that the volume change due to hydrolysis has an effect on the residual stress formation in the surface region. However, the measurements are carried out immediately after the completion of the laser treatment process; therefore, this affect is expected to be insignificant.

Fig. 5 shows friction coefficient of the laser treated and untreated surfaces. Laser treatment lowers the friction coefficient at the surface, which is associated with enhancement of surface microhardness after the laser treatment process. Laser treatment increases the microhardness of the surface; in which case, microhardness of the untreated surface is 11.2 ± 0.2 HV and laser treated surface is 25.1 ± 0.9 HV. It should be noted that microhardness

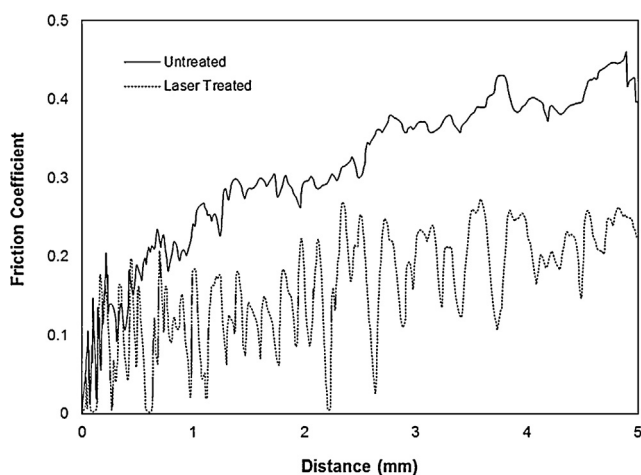


Fig. 5. Friction coefficient along the laser treated and untreated surfaces.

measurements were repeated 10 times at different locations on the laser treated surface and the error estimated from the hardness data is in the order of 0.9 HV. Microhardness variation at the surface is associated with the non-uniform cooling rates and non-uniform distribution of crystal sizes at the surface. However, microhardness enhancement is associated with the crystal structures formed at the surface and high cooling rates, which lowers the crystal size in the surface region; consequently, a dense crystalline surface is resulted after the laser treatment process. The scar sizes are almost uniform and the scar depth is shallower for the laser treated and untreated surfaces. The laser treated surface results in shallow scar depth, which is due to increased hardness at the surface, and no cracks are observed around the scar mark for the laser treated and untreated surfaces. This demonstrates that the surface fracture toughness reduction due to surface hardness enhancement is not significant. Eq. (3) is used to determine the scratch hardness for laser treated and untreated surfaces. It is found that the scratch hardness of the laser treated and untreated surfaces are 110 ± 11 MPa and 80 ± 3.2 MPa, respectively. The scratch tests were conducted at different regions at the laser treated and untreated surfaces. Based on the repeatability of the data, the estimated error is in the order of 6% for the laser treated surface and 4% for the untreated surface.

3.3. Surface morphology, hydrophobicity, and transmittance

Fig. 6 shows AFM images of the laser treated surface. Since laser beam irradiates the surface with high frequency, overlapping of laser spots take place along the laser scanning tracks. Crystallization from the molten state at the cavity surface and melt flow from the newly formed cavity site toward the previously formed cavity lower the cavity depth and alter the geometric features at the irradiated surface. Consequently, micro/nanosize pores are formed at the surface. The spherules have non-spherical morphology indicating crystals grow mainly in multidimensional way at the surface. However, few spherules show open-structured feature, which are not often observed under the chemical crystallization conditions [44]. The roughness of the laser treated surface is in the order of $0.6 \mu\text{m}$, which changes slightly in different directions at the laser treated surface. This is associated with the non-uniform crystallization and laser texturing at the surface.

Fig. 7 and shows the sample images of droplets, which are used for the contact angle measurements on the laser treated and untreated surfaces. One of the parameters for the wettability of solid surfaces by liquids is the contact angle. Although the contact angle of a liquid on a perfectly smooth and chemically homogeneous solid surface can be determined by Young's equation [45], the equation is limited to extremely smooth and homogenous surfaces. Therefore, the Wenzel and Cassie-Baxter equations for apparent contact angle that includes surface roughness should be used [45]. When the liquid impales the roughness features the droplet is said to be in the Wenzel state and the apparent contact angle is given by:

$$\cos \theta_w = \frac{r(\gamma_{sv} - \gamma_{sl})}{\gamma_{lv}} \quad (4)$$

where θ_w is the rough surface contact angle, γ_{sv} is the interfacial tensions of solid-vapor, γ_{sl} is the interfacial tensions of solid-liquid, γ_{lv} is the interfacial tensions of liquid-vapor, r is the surface roughness factor, which is defined as the ratio between the actual and projected surface areas, i.e. $r = 1$ is the perfectly smooth surface and $r > 1$ represents the rough surface.

When the droplet is in the Cassie-Baxter state, a composite interface exists between the droplet and the solid surface. The interface consists of liquid-solid and liquid-vapor interfaces; therefore, the contact angle should include the contributions of

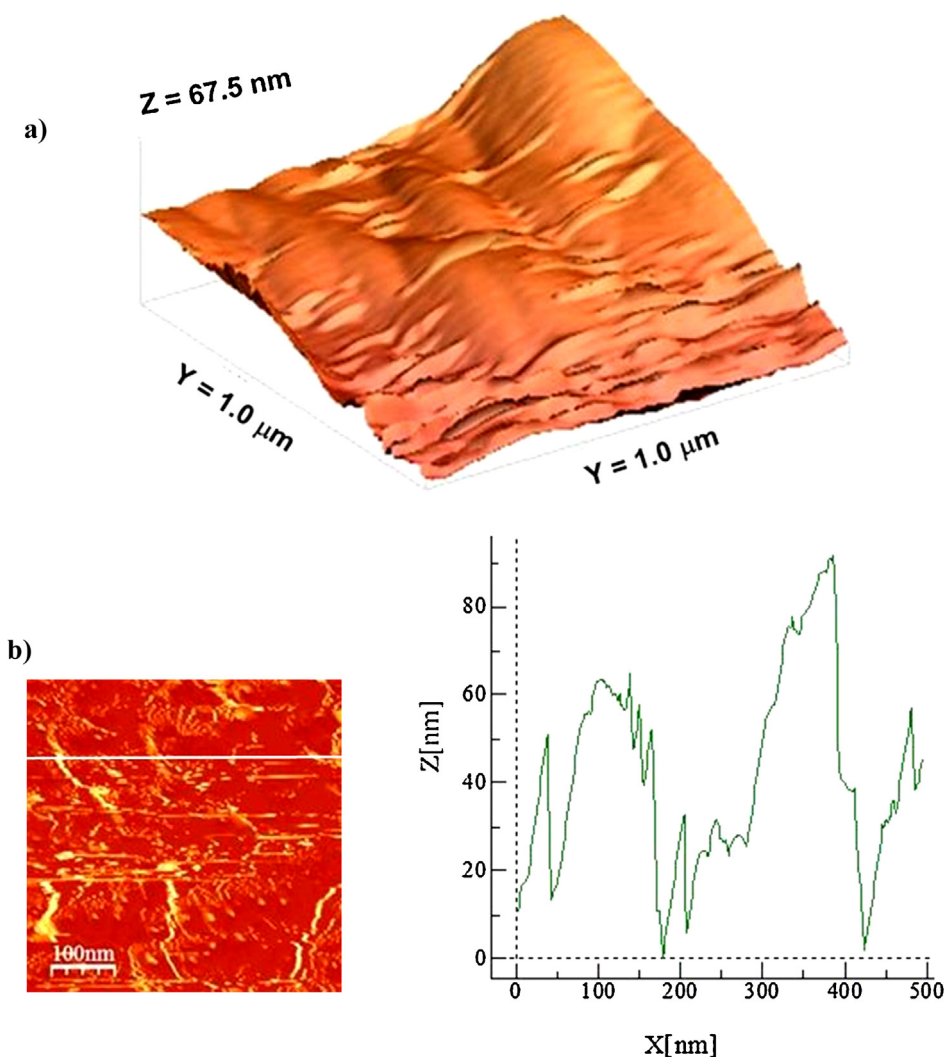


Fig. 6. AFM images of laser treated surface: (a) 3-dimensional view of laser treated surface, (b) imaged use for surface roughness, and (c) surface roughness along the line shown in the image.

two-interfaces. Hence, the equation for the contact angle yields [45]:

$$\cos \theta_c = f_1 \cos \theta_1 + f_2 \cos \theta_2 \quad (5)$$

where θ_c is the apparent contact angle, f_1 is the surface fraction of liquid–solid interface, f_2 is the surface fraction of liquid–vapor interface, θ_1 is the contact angle for liquid–solid interface, and θ_2 is the contact angle for liquid–vapor interface. For the air–liquid interface, f_1 can be represented as f , which is the solid fraction, and air fraction (f_2) becomes $(1 - f)$. The parameter f ranges from 0 to 1; in which case, $f=0$ is the case where the liquid droplet is not in contact with the surface and $f=1$ is case where the surface is completely wetted. It was reported that in the Cassie–Baxter state [46], the small contact area between the liquid droplet and solid surface allowed the droplet to roll easily off surface. In practice, the contact mode changes from Cassie–Baxter state to Wenzel state [47] when the surface texture becomes sparse or when the droplets impact the surface with high velocity [48]. In general, the laser treated surface demonstrates Cassie–Baxter state [46]; in which case, surface texture with low roughness results in air pockets occupying the texture gap while generating hydrophobic behavior at the surface. This situation can be observed from the small value of hysteresis ($\theta_{Advancing} - \theta_{Receding}$, where $\theta_{Advancing}$ is the advancing angle and $\theta_{Receding}$ is the receding angle) for the low roughness surface

(Table 2). However, in some region at the laser treated surface, texture changes and surface roughness increases, which results in non-hydrophobic behavior of the surface, i.e. attainment of high value of hysteresis (Table 2). This occurs randomly and the total coverage area of this region is small at the laser surface. Consequently, mixture of hydrophobic states consisting of Cassie–Baxter, and Wenzel states occur at the laser treated surface. The contact angle measurements reveal that laser treated surface demonstrates hydrophobicity across the large area, which can be observed from Table 2, in which the contact angle data are provided. The roughness factor (f) should be within $0 \leq f \leq 1$ for the hydrophobic surfaces in accordance with Eq. (5). However, superhydrophobicity is only possible for f values approaching to zero. Therefore, f should approach

Table 2
Contact angles measurement results prior to and after the laser treatment.

	Contact angle (°)	
	Low roughness	High roughness
Laser treated surface		
Advancing	128.2 (+5/–5)	92.3 (+5/–5)
Receding	121.2 (+5/–5)	78.5 (+5/–5)
Untreated surface		
Advancing	84.2 (+5/–5)	–
Receding	56.6 (+5/–5)	–

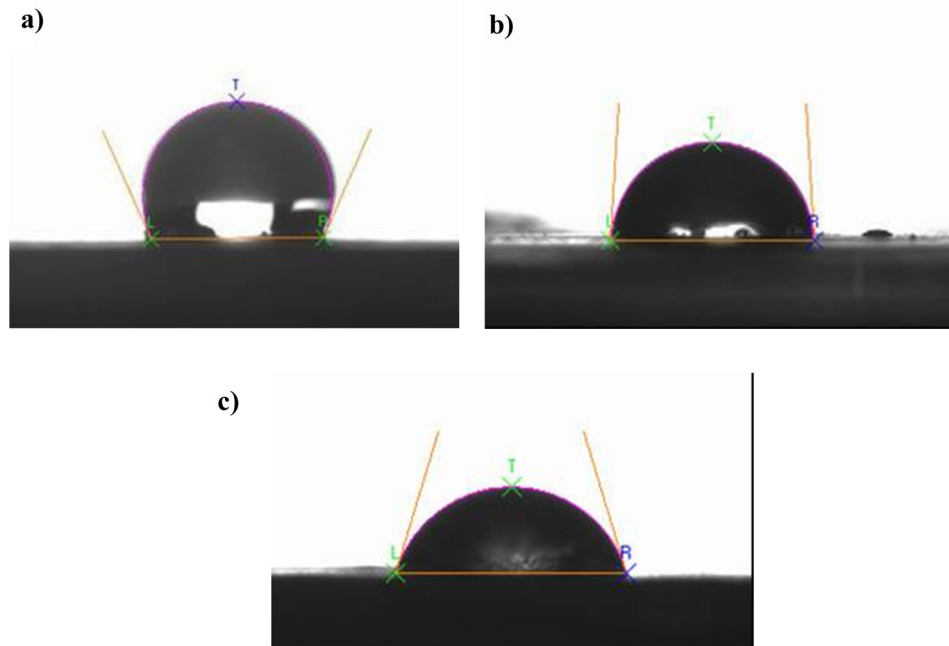


Fig. 7. Optical images used for contact angle measurements, (a) 125° contact angle at the laser treated surface, (b) 86.5° contact angle at the laser treated surface, and (c) 68.4° contact angle at the untreated surface.

0 for large contact angles in the Cassie and Baxter state. This situation is possible when the surface texture comprises mixture of micro/nano size dimples and pillars, which in turn gives rise to the Cassie and Baxter state with large contact angles. This situation is observed in few locations at the laser treated surface; in which case, contact angles well excess of 140° are resulted.

Fig. 8 shows the optical transmittance of the laser treated and untreated surfaces. Laser treated surface has less transmittance than that corresponding to untreated surface. This is associated with the crystal formation at the surface, which alters the absorption characteristics of the incident radiation as evident from FTIR data (Fig. 4). Nevertheless, the maximum reduction in the transmittance is in the order of 15%, which is significantly low as compared to the crystallized surface by the chemical processes, such as immersion in acetone [49]. Almost a linear relation is present between the amount of incident solar radiation received and the photovoltaic device output power [50]. Consequently, using the laser treated protective glass surface lowers 15% of the photovoltaic device output in the short term; however, it is expected to improve significantly device output power in the long term when

dust accumulation prevents the incident solar radiation reaching at the device active surface area.

4. Conclusion

Surface texturing of polycarbonate glass is carried out via controlled laser ablation to enhance the hydrophobicity of the surface. Topology and texture of the resulting surface are examined using optical, scanning electron, atomic force microscopes. Optical and mechanical properties including microhardness and scratch resistance of the surface are evaluated using Fourier transform infrared spectroscopy and micro-tribometer. Residual stress formed in the laser treated layer is determined using the curvature method. Surface hydrophobicity is assessed through contact angle measurements. Thermal analysis is used to estimate the crystallinity at the laser treated surface. Laser ablation results in surfaces composing of micro/nanosize pores and shallow fine-size cavities. Melt layer formed at the cavity surface triggers crystallization of polycarbonate during the cooling period, which in turn modifies the optical characteristics of the treated surface and contributes to the surface texture. The crystallinity estimated from the X-ray data is in the order of 18%, which is significantly higher than that reported for the electrochemical crystallization such as acetone immersion. Crystal growth extends radially from the potential nucleation site; however, in some region intermittent branching occurs. Few partially formed spherules takes place, which are locally scattered at the laser treated surface. In addition, some of spherules formed have non-spherical morphology due to multidimensional crystal growth at the surface. Microhardness of the surface increases two-fold after the laser treatment process, which is associated with high cooling rates and contribution of crystallinity-inducing polymer chains, which are more closely packed and can cause restriction group vibration. Residual stress determined from the curvature method reveals that residual stress is compressive in the laser treated layer and it is in the order of –16 MPa. The findings of scratch tests demonstrate that the scar depth is slightly larger for the untreated surface than that of the laser treated surface indicating the improvement of microstructural integrity in the

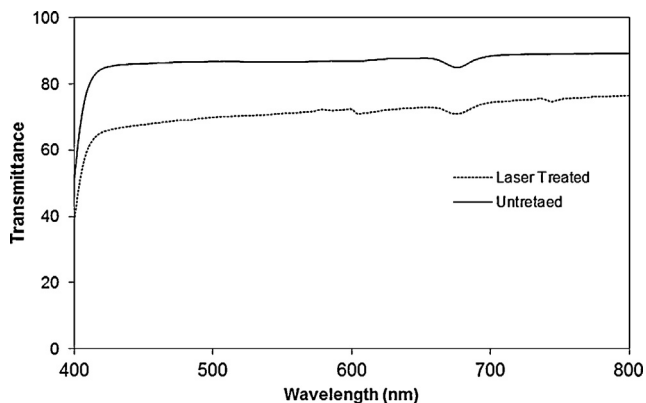


Fig. 8. Transmittance data for laser treated and untreated workpieces.

surface region of the laser treated workpiece. The scratch hardness of the laser treated and untreated surfaces are 110 ± 11 MPa and 80 ± 3.2 MPa, respectively. Laser treated surface demonstrates lower transmittance compared to that corresponding to untreated surface; in which case, the maximum reduction in transmittance is in the order of 15%. This is associated with the crystal formation at the surface, which alters the absorption characteristics of the incident radiation.

Acknowledgements

The authors acknowledge the financial support of King Fahd University of Petroleum and Minerals (KFUPM) through Project# MIT11111-11112, and King Abdulaziz City for Science and Technology (KACST) through project# 11-ADV2134-04 to accomplish this work.

References

- [1] J.C. Bird, R. Dhiman, H.-M. Kwon, K.P. Varanasi, Reducing the contact time of a bouncing drop, *Nature* 503 (2013) 385–388.
- [2] S. Anand, A.T. Paxson, R. Dhiman, J.D. Smith, K.K. Varanasi, Enhanced condensation on lubricant-impregnated nanotextured surfaces, *ACS Nano* 6 (11) (2012) 10122–10129.
- [3] H. Jing, Y. Higaki, W. Ma, J. Xi, H. Jinnai, H. Otsuka, A. Takahara, Preparation and characterization of polycarbonate nanocomposites based on surface-modified halloysite nanotubes, *Polym. J.* 46 (2014) 307–312.
- [4] A. Nakajima, Design of hydrophobic surfaces for liquid droplet control, *NPG Asia Mater.* 3 (2011) 49–56.
- [5] K.-C. Park, H.J. Choi, C.-H. Chang, R.E. Cohen, G.H. McKinley, G. Barbastathis, Nanotextured silica surfaces with robust superhydrophobicity and omnidirectional broadband supertransmissivity, *ACS Nano* 6 (5) (2012) 3789–3799.
- [6] M. Nosonovsky, B. Bushan, Capillary effects and instabilities in nanocontacts, *Ultramicroscopy* 108 (2008) 1181–1185.
- [7] T. Wagner, C. Neinhuis, W. Barthlott, Wettability and contaminability of insect wings as a function of their surface sculptures, *Acta Zool.* 77 (3) (1996) 213–225.
- [8] A.R. Parker, C.R. Lawrence, Water capture from desert fogs by a Namibian beetle, *Nature* 414 (6859) (2001) 33–34.
- [9] X. Gao, L. Jiang, Biophysics, Water-repellent legs of water striders, *Nature* 432 (7013) (2004) 36.
- [10] D. Byun, J. Hong, Saputra, J.H. Ko, Y.J. Lee, H.C. Park, B.K. Byun, J.R. Lukes, Wetting characteristics of insect wing surfaces, *J. Bionic Eng.* 6 (1) (2009) 63–70.
- [11] K. Koch, B. Bhushan, W. Barthlott, Diversity of structure, morphology and wetting of plant surfaces, *Soft Matter* 4 (10) (2008) 1943–1963.
- [12] M. Callies, D. Quere, On water repellency, *Soft Matter* 55 (1) (2005) 55–61.
- [13] J.T. Han, X.R. Xu, K.W. Cho, Diverse access to artificial superhydrophobic surfaces using block co-polymers, *Langmuir* 21 (15) (2005) 6662–6665.
- [14] N.J. Shirtcliffe, G. McHale, M.I. Newton, G. Chabrol, C.C. Perry, Dual-scale roughness produces un-usually water-repellent surfaces, *Adv. Mater.* 16 (21) (2004) 1929–1932.
- [15] H.S. Hwang, S.B. Lee, I. Park, Fabrication of rasp-berry-like superhydrophobic hollow silica particles, *Mater. Lett.* 64 (20) (2010) 2159–2162.
- [16] Y.H. Huang, J.T. Wu, S.Y. Yang, Direct fabricating patterns using stamping transfer process with PDMS mold of hydrophobic nanostructures on surface of micro cavity, *Microelectron. Eng.* 88 (6) (2011) 849–854.
- [17] T. Yang, H. Tian, Y. Chen, Preparation of superhydrophobic silica films with honeycomb-like structure by emulsion method, *J. Sol-Gel Sci. Technol.* 49 (2) (2009) 243–246.
- [18] H. Kinoshita, A. Ogasahara, Y. Fukuda, N. Ohmae, Superhydrophobic/superhydrophilic micropatterning on a carbon nanotube film using a laser plasma-type hyperthermal atom beam facility, *Carbon* 48 (15) (2010) 4403–4408.
- [19] S.S. Latthe, H. Imai, V. Ganesan, A.V. Rao, Super-hydrophobic silica films by sol-gel co-precursor method, *Appl. Surf. Sci.* 256 (1) (2009) 217–222.
- [20] M. Ma, Y. Mao, M. Gupta, K.K. Gleason, G.C. Rutledge, Superhydrophobic fabrics produced by electrospinning and chemical vapor deposition, *Macromolecules* 38 (23) (2005) 9742–9748.
- [21] X. Zhang, Y. Guo, P. Zhang, Z. Wu, Z. Zhang, Superhydrophobic CuO/Cu₂S nanoplate vertical arrays on copper surfaces, *Mater. Lett.* 64 (10) (2010) 1200–1203.
- [22] B.S. Yilbas, M. Khaled, N. Abu-Dheir, N. Aqeeli, S.Z. Furquan, Laser texturing of alumina surface for improved hydrophobicity, *Appl. Surf. Sci.* 286 (2013) 161–170.
- [23] F.L.B.O. de Oliveira, M.C.A.M. Leite, L.O. Conto, T.R. Correia, Study on bisphenol-A polycarbonates samples crystallized by acetone vapor induction, *Polym. Bull.* 67 (2011) 1045–1057.
- [24] Y. Zhou, Y. Dan, L. Jiang, G. Li, The effect of crystallization on hydrolytic stability of polycarbonate, *Polym. Degrad. Stab.* 98 (8) (2013) 1465–1472.
- [25] I. Yilgor, S. Bilgin, M. Isik, E. Yilgor, Facile preparation of superhydrophobic polymer surfaces, *Polymer* 53 (6) (2012) 1180–1188.
- [26] F. Palumbo, R. Di Mundo, D. Cappelluti, R. Dagostino, Superhydrophobic and superhydrophilic polycarbonate by tailoring chemistry and nano-texture with plasma processing, *Plasma Process. Polym.* 8 (2) (2011) 118–126.
- [27] Y. Cui, A.T. Paxson, K.M. Smyth, K. Varanasi, Hierarchical polymeric textures via solvent-induced phase transformation: a single-step production of large-area superhydrophobic surfaces, *Colloids Surf. A: Physicochem. Eng. Asp.* 394 (2012) 8–13.
- [28] S. Li, A.H. Barber, Creating superhydrophobic polycarbonate fiber network from hydrophilic polycarbonate through electrospinning, *Mater. Res. Soc. Symp. Proc.* 1403 (2012) 53–58.
- [29] S.M. Hurst, B. Farshchian, J. Choi, J. Kim, S. Park, A universally applicable method for fabricating superhydrophobic polymer surfaces, *Colloids Surf. A: Physicochem. Eng. Asp.* 407 (2012) 85–90.
- [30] S.K. Papadopoulou, C. Tsiptsias, A. Pavlou, K. Kaderides, S. Sotiriou, C. Panayiotou, Superhydrophobic surfaces from hydrophobic or hydrophilic polymers via nanophase separation or electrospinning/electrospraying, *Colloids Surf. A: Physicochem. Eng. Asp.* 387 (1–3) (2011) 71–78.
- [31] J.T. Han, J.S. Kim, S.H. Kim, H.S. Lim, H.J. Jeong, S.Y. Jeong, G.-W. Lee, Nanocarbon induced rapid transformation of polymer surfaces into superhydrophobic surfaces, *ACS Appl. Mater. Interfaces* 2 (11) (2010) 3378–3383.
- [32] T.C. Totemeier, R.N. Wright, Residual stress determination in thermally sprayed coatings—a comparison of curvature models and X-ray techniques, *Surf. Coat. Technol.* 200 (12–13) (2006) 3962–3995.
- [33] S. Go, M. Han, Y. Ahn, Formation of nanoporous polycarbonate surfaces and their chemical modification for superhydrophobicity, *Bull. Korean Chem. Soc.* 33 (11) (2012) 3899–3902.
- [34] J.I. Lauritzen Jr., J.D. Hoffman, Theory of formation of polymer crystals with folded chains in dilute solution, *J. Res. Natl. Bur. Stand.* 64A (1960) 73.
- [35] F.C. Frank, M. Tosi, On the theory of polymer crystallization, *Proc. R. Soc. (London)* A263 (1961) 323.
- [36] J.D. Hoffman, Thermodynamic driving force in nucleation and growth processes, *J. Chem. Phys.* 29 (1958) 1192.
- [37] J.D. Hoffman, J.I. Lauritzen Jr., Crystallization of bulk polymers with chain folding: theory of growth of lamellar spherulites, *J. Res. Natl. Bur. Stand.* 65A (1961) 297.
- [38] Z. Fan, C. Shu, Y. Yu, V. Zaporozhtchenko, F. Faupel, Vapor-induced crystallization behavior of bisphenol-A polycarbonate, *Polym. Eng. Sci.* 46 (6) (2006) 729–734.
- [39] B.S. Hsiao, K.H. Gardner, D.Q. Wu, B. Chu, Time-resolved X-ray study of poly(aryl ether ether ketone) crystallization and melting behaviour. 2. Melting, *Polymer* 34 (19) (1993) 3996–4003.
- [40] A. Alizadeh, S. Sohn, J. Quinn, H. Marand, L. Shank, H.D. Iler, Influence of structural and topological constraints on the crystallization and melting behavior of polymers. 3. Bisphenol a polycarbonate, *Macromolecules* 34 (12) (2001) 4066–4078.
- [41] H. Marand, A. Alizadeh, R. Farmer, R. Desai, V. Velikov, Influence of structural and topological constraints on the crystallization and melting behavior of polymers. 2. Poly(arylene ether ether ketone), *Macromolecules* 33 (May (9)) (2000) 3392–3403.
- [42] R.M. Silverstein, C.G. Bassler, T.C. Morrill, *Spectroscopic Identification of Organic Compounds*, John Wiley and Sons, New York, 1991.
- [43] W. Zhao, S. Barsun, K. Ramani, T. Johnson, R. King, S. Lin, Development of PMMA-precoating metal prostheses via injection molding: residual stresses, *J. Biomed. Mater. Res.* 58 (4) (2001) 456–462.
- [44] Y.H. Cui, A.T. Paxson, K.M. Smyth, K.K. Varanasi, Superhydrophobic polymer surface via solvent-induced crystallization, in: 13th IEEE ITherm Conference, Paper no. 978-1-4244-9532-0, 2012, pp. 951–955.
- [45] Y.C. Jung, B. Bhushan, Wetting transition of water droplets on superhydrophobic patterned surfaces, *Scr. Mater.* 57 (12) (2007) 1057–1060.
- [46] A.B.D. Cassie, S. Baxter, Wettability of porous surfaces, *Trans. Faraday Soc.* 40 (1944) 546–551.
- [47] R.N. Wenzel, Resistance of solid surfaces to wetting by water, *Ind. Eng. Chem.* 28 (8) (1936) 988–994.
- [48] T. Deng, K. Varanasi, M. Hsu, N. Bhate, C. Keimel, J. Stein, M. Blohm, Nonwetting of impinging droplets on textured surfaces, *Appl. Phys. Lett.* 94 (2009), <http://dx.doi.org/10.1063/1.3110054>.
- [49] A.O.M. Ahmed, Design and fabrication of different textured surfaces with improved hydrophobicity for photovoltaic cells' applications (MS Thesis), Chemistry Department, KFUPM, 2014.
- [50] P. Attaviriyanupap, K. Tokuhara, N. Itaya, M. Marmioli, Estimation of photovoltaic power generation output based on solar irradiation and frequency classification, in: Proceedings of Innovative Smart Grid Technologies Asia (ISGT), 2011 IEEE PES, Perth, Western Australia, 13–16 November, 2011, pp. 1–7.